nature communications

Article

https://doi.org/10.1038/s41467-025-57598-9

GCN5-targeted dual-modal probe across the blood-brain barrier for borders display in invasive glioblastoma

Received: 21 November 2023

Accepted: 27 February 2025

Published online: 08 March 2025

Check for updates

Haiyan Zheng[1,4], Lu Zhang[2,4], Xinning Bai[1,4], Jinchao Zhu[1,4], Shanshan Liu[3,4], Yao Ke[1], Qingyuan Lin[1], Yuan Yuan[1] & Tianhai Ji[1]

Glioblastoma (GBM) is a highly invasive malignancy with a poor prognosis, primarily attributable to its diffuse infiltration into adjacent brain tissue, thereby complicating effective surgical resection. Current imaging modalities often struggle to accurately identify tumor boundaries. Here, we identify general control non-repressed protein 5 (GCN5) as a promising molecular target for GBM imaging, as it is expressed in GBM lesions within brain tissue, and its expression levels are significantly correlated with GBM grading. We develop a dual-modal probe with a particle size of 20 nm, capable of efficiently traversing the blood-brain barrier (BBB) to target GCN5 through adsorptive-mediated transcytosis (AMT). The probe employs dendrimers (Den) as carriers, which are loaded with a small molecule inhibitor specifically designed to target GCN5. This probe enhances the preoperative delineation of GBM boundaries using magnetic resonance imaging (MRI) and facilitates intraoperative fluorescence image-guided surgical procedures. Our work introduces a promising tool for boundary delineation, offering new opportunities for the precise resection of GBM.

Glioblastoma (GBM) is the most common malignant brain tumor of the central nervous system, with an incidence rate of 5.8 per 100 000 persons. The five-year survival rate for GBM is below 10%, with the median survival duration for patients being approximately 14.6 months[1,2]. Because of the blood–brain barrier (BBB) and the tumor's heterogeneity[3], GBM is invariably unresponsive to conventional chemotherapy and radiotherapy, with surgical resection being the best frontline treatment option. GBM cells infiltrate adjacent brain tissue in a crab-like fashion, forming networks with tumor micro-vessels through ultra-long thin protrusions[4,5]. Consequently, surgeons typically struggle to distinguish the tumor border from the surrounding normal brain tissue, resulting in incomplete resection of tumor cells during surgery[6]. Within 8–12 months post-surgery, the majority of GBM typically recur at the edge of the resection cavity[4]. The imperative for a non-invasive imaging technology capable of precisely delineating the margin between GBM and normal brain tissue for surgical guidance is therefore unequivocally apparent[7].

Magnetic resonance imaging (MRI) using contrast agents is the preferred method for the preoperative detection of GBM. However, accurately delineating small GBM lesions remains challenging due to insufficient sensitivity. While commercially available clinical contrast agents have enhanced the MRI diagnostic efficiency in many cancer types, they have shown limited effectiveness in GBM diagnosis due to restricted BBB permeability and reduced in vivo circulation durations[8]. Gadolinium (Gd)-based contrast agents have been widely employed in MRI for the GBM diagnosis[9]. Fluorescence image-guided surgery (FGS) utilizing fluorescent probes such as 5-aminolevulinic acid (5-ALA) and the US Food and Drug Administration (FDA) approved indocyanine green (ICG)[10–13], has demonstrated improved tumor resection outcomes during surgery[14]. The integration of MRI and fluorescence

[1]Department of Pathology, Shanghai Ninth People's Hospital, Shanghai Jiao Tong University School of Medicine, Shanghai, China. [2]Nuclear Medical Department, Changhai Hospital affiliated to Naval Medical University, Shanghai, China. [3]Chenggong Hospital, Xiamen University, Xiamen, China. [4]These authors contributed equally: Haiyan Zheng, Lu Zhang, Xinning Bai, Jinchao Zhu, Shanshan Liu. e-mail: skysea_ji@sina.com

imaging facilitates the delineation of GBM boundaries for preoperative localization and image-guided surgical intervention.

Conventional contrast agents exhibited limited BBB permeability and reduced circulation durations in vivo. Recently, the development of nanoparticles (NPs) has offered a promising new approach for the diagnosis and treatment of GBMs, which can be chemically modified and bio-conjugated with versatile molecules or peptides to improve BBB penetration, target tumors, and enable multi-modal imaging[15,16]. Dendrimer (Den) possesses molecular extensions, functional molecular architecture, and the ability to penetrate the BBB, it is thus applied in imaging and treatment studies of GBMs[17]. A straightforward modification could significantly improve the permeability of Den across the BBB[18].

To enhance the tumor-targeting specificity of imaging probes, existing biological studies have utilized biomolecules that bind to tumor-specific biomarkers for the labeling of imaging probes[19–21]. The epidermal growth factor receptor (EGFR) is overexpressed in 60–90% of GBMs[22].The EGFR inhibitor Cetuximab has been conjugated with MRI contrast agents to obtain Fe3O4@Au-C225, shows good targeting ability on GBM imaging[23]. The folic acid receptor (FAR) is expressed at low levels in normal tissues, but is overproduced in brain tumors and the BBB, and is also used as a marker for GBM imaging[24].

We previously demonstrated that lysine acetyltransferase 2 A (KAT2A, also known as GCN5) is highly expressed in GBM[25]. In this context, we utilized multi-omic techniques for an in-depth investigation and identified that GCN5 is highly expressed in GBMs and is associated with tumor grading, while it is not expressed in normal brain tissue. This fully demonstrates the potential of GCN5 as a biomarker for the molecular imaging of GBMs.

In this work, we develop an MRI/NIR dual-modal imaging probe, ICG-Gd-Den @DC-G16-11, achieving precise delineation of the boundaries of GBM by targeting GCN5 within the tumor. As a carrier, we select the PEG-modified dendritic polymer material, Den. Initially, Den is conjugated with the chelating agent dodecane tetraacetic acid (DOTA) and subsequently with the MRI contrast agent Gd before being linked to the small-molecule inhibitor DC-G16-11, a specific inhibitor targeting GCN5 with relatively high activity[26], and ICG[27] to form a dual-modal probe. This probe possesses a particle size of 20 nm and carries a positive charge, enabling it to traverse the BBB via the adsorptive-mediated transcytosis (AMT) pathway[28]. The dual-modal probe facilitates both preoperative MRI and intraoperative NIR fluorescence imaging, allowing for precise tumor delineation at variou time points. The probe's specificity for targeting GBM enhances the specific accumulation of the tumor and prolongs the retention time of the probe within the tumor, thereby improving imaging effectiveness. This finding has the potential to aid clinicians in the precise removal of residual GBM lesions, consequently reducing the rate of postoperative recurrence.

Results

GCN5 is highly expressed in high-grade gliomas

To identify significant molecular markers for the malignant evolution of gliomas, we analyzed clinical information and transcript expression data from 749 glioma cases obtained from the Chinese Glioma Genome Atlas (CGGA) database. Clustered heatmap analysis revealed that GCN5 expression was significantly correlated with glioma World Health Organization (WHO) grade, patient age, and IDH1 mutation status (Fig. 1a). Differential expression analysis further demonstrated a positive association between GCN5 expression and glioma malignancy, with the highest expression observed in WHO grade IV glioblastomas (GBMs) (Fig. 1b). This finding suggests that GCN5 might be linked to glioma proliferation and invasion.

To validate these observations, we first confirmed through western blotting and immunofluorescence that GCN5 is widely expressed in various GBM cell lines, localizing to both the nucleus and cytoplasm (Supplementary Fig. 1a, c). Functional analysis demonstrated that overexpression of GCN5 enhances the colony-forming ability of GBM cells, while its knockdown significantly suppresses this ability, further supporting its role in GBM proliferation (Supplementary Fig. 1b). To confirm the actual expression of GCN5 in patients with glioma, we analyzed 87 glioma samples using tissue microarrays. Immunohistochemistry (IHC) results showed that GCN5 expression was significantly increased in GBM tissues compared to lower-grade gliomas and was localized in the cytoplasm, while it was almost not expressed in normal brain tissue (Fig. 1c, d). The clinical information of the 87 glioma patients and the expression levels of GCN5 are detailed in supplementary Tables 1 and 2. Based on these findings, GCN5 is confirmed as a potential molecular imaging marker for accurately defining the boundaries of GBMs.

Construction and characterization of dual-modal probe targeting GCN5-overexpressed GBMs

In this study, we utilized PAMAM G2-NH2 dendrimers (Den) to construct the dual-modal probe. Previous study has shown that the positively charged terminal amines of Den can interact with cellular membranes, this interaction facilitates cellular entry by forming nanoscale pores in the cell membrane and can even allow crossing of the nuclear membrane to access the cell nucleus[29,30]. Some research has confirmed that DC-G16-11 efficiently targets GCN5 and is a promising chemical probe[26], with the chemical structure shown in Supplementary Fig. 2. Thus, we modified the Den using polyethylene glycol (PEG) and conjugated it with contrast agents DOTA-Gd, NHS-ICG, and DC-G16-11 in turn, producing a dual-modal probe targeting GCN5 overexpressed GBM for MRI and fluorescent imaging simultaneously, named ICG-Gd-Den@DC-G16-11 (Fig. 2a). Afterwards, scanning transmission electron microscopy (STEM) demonstrated that the probes had uniform morphology (Fig. 2b).

To validate element distribution of probe, we further employed STEM to evaluate the energy distribution of Gd atoms using energy-dispersive X-ray spectroscopy elemental analysis, and the Gd atoms were depicted as yellow vector points in Fig. 2c. These yellow vector points concur with the observed particles in overlap of STEM and elemental mapping of ICG-Gd-Den@DC-G16-11 (Fig. 2d), emphasizing their substantial accumulation in the distribution zone of dendritic structure. The content of Gd ion on per milligram Den was measured about to $74.91 \pm 7.18\ \mu g\ mg^{-1}$ by ICP-OES. Taken together, we speculated that the surface of the dendritic probe effectively sequestered Gd ion.

The particle size of probe was about to 19.45 ± 7.76 nm (Fig. 2e), with a positively charged of 26.04 ± 3.36 mV on the surface (Fig. 2f), and a steady dispersion of the probe in DMEM containing 10% Fetal Bovine Serum (FBS) to stimulate physiological condition (Fig. 2g). To confirm the specificity of ICG-Gd-Den@DC-G16-11 for targeting GCN5, we employed surface plasmon resonance (SPR) technology and software fitting to determine that the dissociation constant (KD) of the probe is 6.8 μM (Fig. 2h), thus corroborating DC-G16-11's good affinity for GCN5 following various modifications.

To demonstrate the probe's capability for MRI imaging, we conducted the longitudinal proton relaxation time (T1)-weighted MRI of the ICG-Gd-Den@DC-G16-11 probe at different Gd ion concentrations. As the Gd ion concentration increased, we observed a gradual rise in positive contrast-to-noise ratio, affirming the probe's exceptional magnetic sensitivity (Fig. 2i). Furthermore, the relaxation rate of the probe at 37°C was calculated to be $10.43\ mM^{-1}S^{-1}$ (Fig. 2j), which was markedly higher than that of commercially available contrast agents such as Magnevist® (Gd-DTPA, $r_1 = 4.9\ mM^{-1}S^{-1}$, 1.5 T magnetic field)[31] and demonstrated a significant enhancement in the imaging performance of ICG-Gd-Den@DC-G16-11 attributed to the surface chelation of several Gd ions on the high-surface-area Den.

We further investigated the optical properties of ICG-Gd-Den@DC-G16-11 using the VISQUE InVivo Smart near-infrared (NIR) animal

https://doi.org/10.1038/s41467-025-57598-9

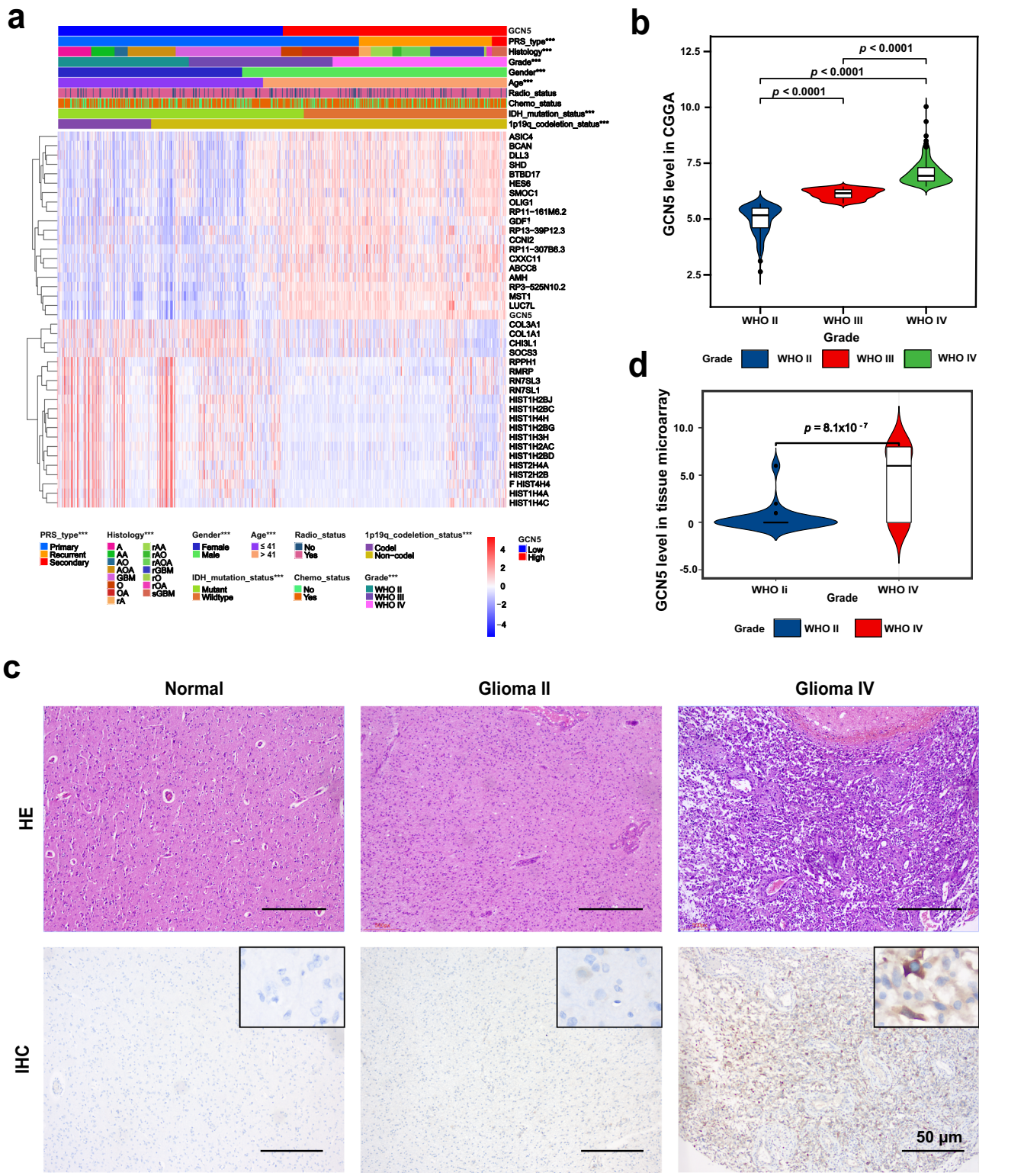

Fig. 1 | GCN5 is highly expressed in high-grade gliomas. a Heatmap clustering shows a significant positive correlation between GCN5 expression and glioma pathological grade, tissue type, patient age, and IDH mutation status, based on Chinese Glioma Genome Atlas (CGGA) database analysis. **b** GCN5 expression levels, derived from 749 glioma samples in the CGGA database, are significantly elevated in World Health Organization (WHO) grade IV GBMs compared to lower-grade gliomas.WHO grade II, $n = 218$ samples (blue); WHO grade III, $n = 240$ samples (red) and WHO grade IV, $n = 291$ samples (green). **c** Representative immunohistochemistry (IHC) images illustrating GCN5 expression in normal brain tissue, low-grade gliomas, and high-grade gliomas. **d** Comparison of GCN5 expression levels in WHO grade II and grade IV gliomas. WHO grade II, $n = 36$ samples (blue); WHO grade IV, $n = 51$ samples (red). The data (**b**) and (**d**) are presented as box - plots and the data distribution characteristics are shown through violin plots. The upper and lower bounds of the box are defined by the 75th and 25th of the data distribution. The median is represented by a bold horizontal line within the box. The whiskers above and below the box are the maximum and minimum values. The *P* value in (**b** and **d**) was calculated by the two-sided Mann-Whitney U test (Wilcoxon rank-sum test). $^{****}p < 0.0001$.

https://doi.org/10.1038/s41467-025-57598-9

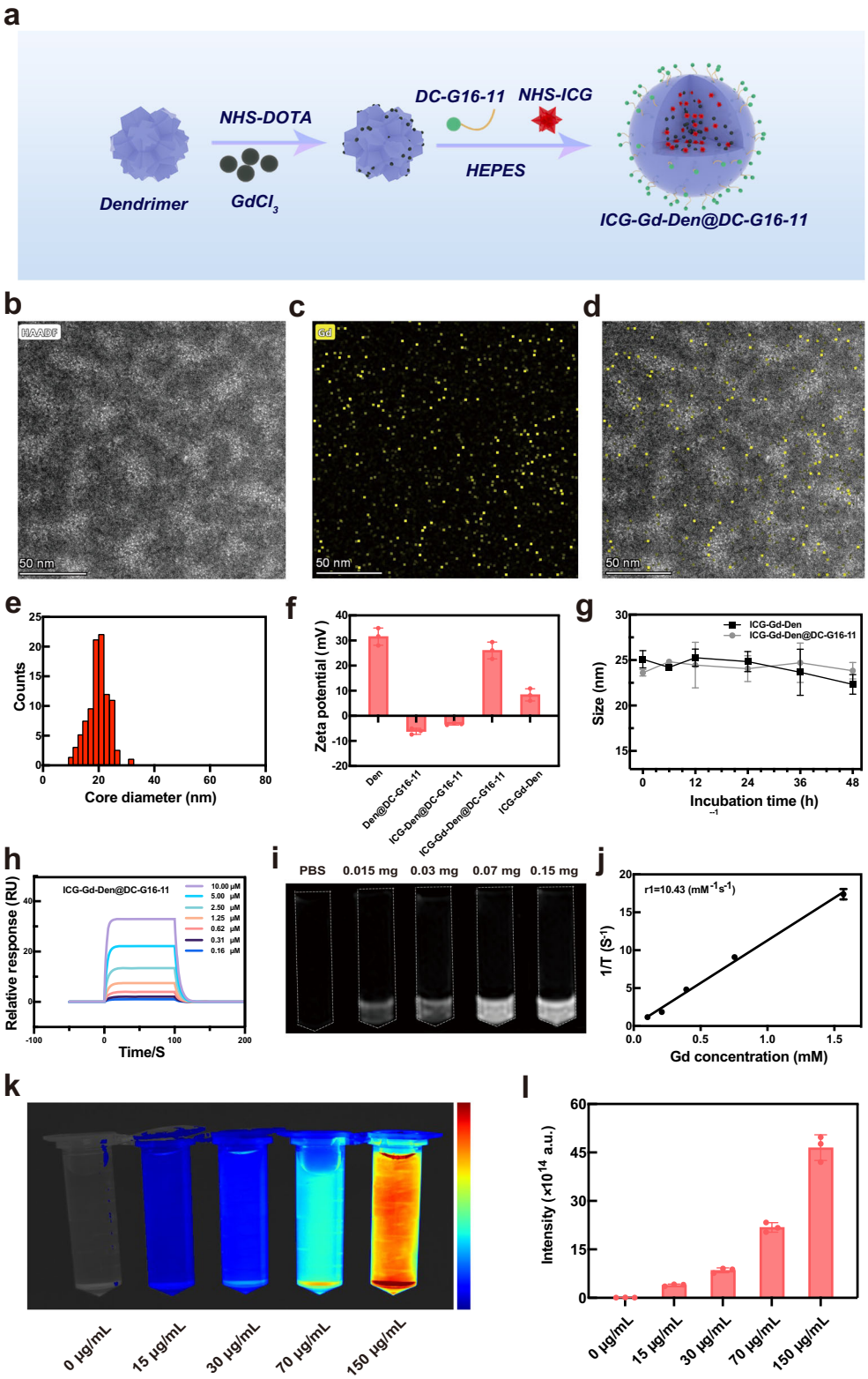

fluorescence imaging system and fluorescence spectrophotometer. The results indicated that a high signal intensity reflected a higher concentration of ICG-Gd-Den@DC-G16-11 in the concentration range tested (Fig. 2k). The maximum emission wavelength was observed at 808 nm, and the probe was evenly distributed in saline solution. This finding indicated that the Den loaded with ICG existed in phosphate-buffered saline (PBS) in a monodispersed form, minimizing aggregation. Additionally, we constructed a semi-quantitative curve depicting the fluorescence intensity of the ICG-Gd-Den@DC-G16-11 against varying Gd ion concentrations, utilizing a fluorescence spectrophotometer. This analysis confirmed a strong linear correlation between fluorescence intensity and Gd concentration (Fig. 2l). These results demonstrated excellent fluorescence responsiveness and optical properties of the probe.

https://doi.org/10.1038/s41467-025-57598-9

Fig. 2 | Construction and characterization of Dual-modal probe targeting GCN5-overexpressed GBM. a Schematic representation of the probe's synthesis. **b** Scanning transmission electron microscopy (STEM) images of the ICG-Gd-Den@DC-G16-11. **c** Energy Dispersive Spectrometer detector (EDS) mapping of Gd ion. **d** Overlap of STEM images and element mapping of the ICG-Gd-Den@DC-G16-11. **e** Particle size distribution of ICG-Gd-Den@DC-G16-11. **f** Variation of zeta potential of ICG-Gd-Den@DC-G16-11 during the modification process ($n = 3$ independent experimental replicates). **g** Alteration of the water-based particle size of ICG-Gd-Den and ICG-Gd-Den@DC-G16-11 probes at different time intervals in high glucose serum DMEM containing 10% FBS ($n = 3$ independent experimental replicates). **h** SPR-based binding assay of ICG-Gd-Den@DC-G16-11 with GCN5. **i** Magnetic resonance T1-weighted imaging of the probe at varying Gd ion concentrations. **j** Fitting curve for the relaxation rate of the probe at different Gd ion concentrations, with r_1 relaxation rate equal to 10.43 $mM^{-1}s^{-1}$ ($n = 3$ independent experimental replicates). **k** Near-infrared fluorescence imaging of the ICG-Gd-Den@DC-G16-11 probe dispersed in PBS at different Gd ion concentrations (808 nm, 1.0 W cm^{-2}). **l** Semi-quantitative curve of fluorescence intensity of ICG-Gd-Den@DC-G16-11 probe against Gd ion concentrations ($n = 3$ independent experimental replicates). Data in (**f**, **g**, **j** and **l**) were presented as mean values ± standard deviation (SD).

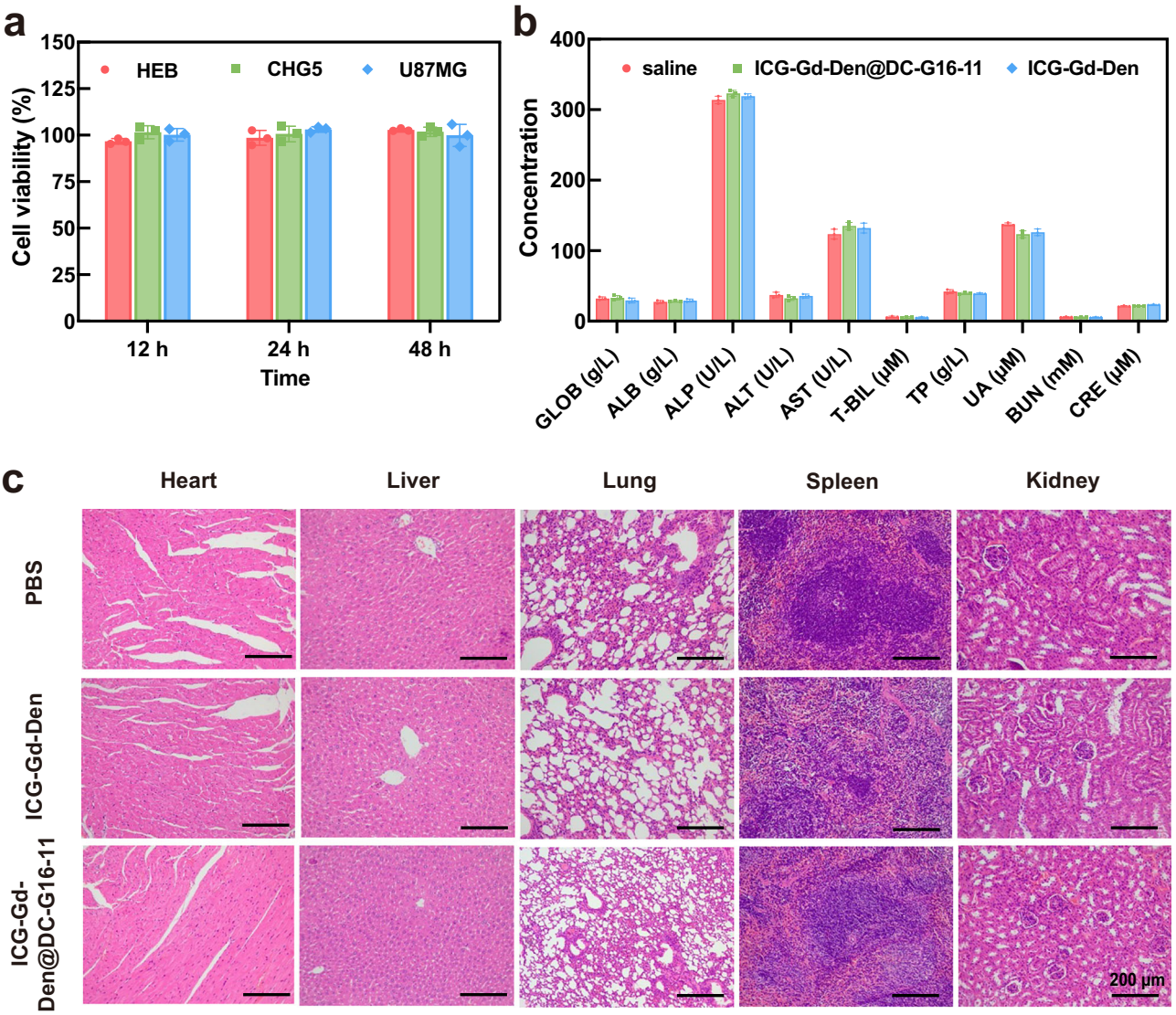

Fig. 3 | Biocompatibility evalution of ICG-Gd-Den@DC-G16-11. a Cytotoxicity of U87 cells, CHG5 cells and HEB cells under 150 μg mL^{-1} concentrations of ICG-Gd-Den@DC-G16-11 (n = 3 independent experimental replicates). **b** Blood chemistry examinations. Globulin (GLOB), albumin (ALB), plasma alkaline phosphatase (ALP), alanine aminotransferase (ALT), and aspartate aminotransferase (AST), total bilirubin(T-BIL), total protein (TP), uric acid (UA), blood urea nitrogen (BUN), creatinine (CRE) levels were assessed after tail vein injection of physiological saline, ICG-Gd-Den@DC-G16-11 and ICG-Gd-Den (100 μL of 20 mg mL^{-1}, Gd concentration: 1.5 mg mL^{-1}). $n = 3$ independent experimental replicates. **c** H&E staining images of main organs (heart, liver, lung, spleen, and kidney) from each group. Data in (**a**, **b**) are presented as mean values ± SD.

Biocompatibility evaluation of ICG-Gd-Den@DC-G16-11

We further evaluated the biocompatibility of the ICG-Gd-Den@DC-G16-11 probe through in vivo and in vitro experiments. First, the ICG-Gd-Den@DC-G16-11 probes were co-cultured with HEB, CHG5, and U87 cell lines at a high concentration of 150 μg mL^{-1} for 12, 24, and 48 h. Methyl Thiazolyl Tetrazolium (MTT) toxicity experiments showed that the cell survival rate did not change significantly (Fig. 3a), indicating no toxic side effects on normal brain cells and GBM cell lines in vitro. We also conducted in vivo toxicological evaluations on healthy mice through blood chemistry indicators and histological examinations,

using saline as the control group. The saline (100 µL), ICG-Gd-Den@DC-G16-11 and ICG-Gd-Den (100 µL of 20 mg mL^{-1}, Gd concentration: 1.5 mg mL^{-1}) were separately injected into healthy mice, and after 7 days, blood was collected from the mice to access liver function biomarkers (globulin (GLOB), albumin (ALB), plasma alkaline phosphatase (ALP), alanine aminotransferase (ALT), and aspartate aminotransferase (AST), total bilirubin(T-BIL), total protein (TP)) and kidney function biomarkers ((uric acid (UA), blood urea nitrogen (BUN), creatinine (CRE)) via chemiluminescence analysis. The results demonstrated that, compared to the control group, ICG-Gd-Den@DC-G16-11 exhibited no toxic side effects on the hepatic or renal systems in mice (Fig. 3b). Subsequently, the mice were euthanized and the main organs were surgically removed (heart, liver, spleen, lung and kidney). After hematoxylin and eosin (H&E) staining, no significant inflammatory reactions or other pathological changes were observed (Fig. 3c). In summary, no noticeable cytotoxicity of ICG-Gd-Den@DC-G16-11 was observed in the biocompatibility study, indicating it as a promising candidate for in vivo biological imaging applications.

BBB-crossing efficiency of dual-modal probes in vitro

Efficiently crossing the BBB is essential for GBM detection using imaging probe[5]. To create an accurate simulation of the probe's penetration rate through the human BBB, we constructed a dynamic co-culture microfluidic biomimetic model of the blood-brain barrier[32]. In this model, astrocytes (HA-1800) were seeded in the upper chamber to establish the neural chamber, and brain microvascular endothelial cells (hCMEC/D3) were seeded upside down in the lower chamber to create the vascular chamber (Fig. 4a). A precise shaker was employed to simulate vascular shear stress, which promoted the expression of ZO-1 protein and strengthened tight junctions between endothelial cells (Supplementary Fig. 3a, b). We measured the transendothelial electrical resistance (TEER) each day as an indicator of BBB permeability to monitor the development of cell fusion and tight connections. Our results indicated that the TEER attained its maximum value on the seventh day after modeling (Fig. 4b). As the BBB barrier function depends on the high expression of specific proteins, particularly tight junction proteins such as ZO-1 in BBB endothelial cells[33], we evaluated ZO-1 expression in the model on the seventh day after modeling using immunofluorescence staining. On the sixth day of modeling, there was a significant upregulation in the expression of the ZO-1 protein (Fig. 4c). This result confirms that tight junctions between vascular endothelial cells have been formed, making it suitable for testing the penetration rate of probes through the BBB. Small molecule penetration experiments were conducted on the sixth day post-model construction to confirm barrier function. Fluorescein sodium solution (FLU, 376 Da) and two FITC-dextran solutions of different molecular weights (40 kDa and 70 kDa) were separately added to the vascular chamber of the model. Samples of the culture medium were collected from the neural chamber, and the fluorescence intensity was measured using a fluorescence spectrophotometer. Subsequently, permeability (Papp) for each model was calculated. The FITC-labeled dextran solutions of 70 kDa, which have a similar particle size to ICG-Gd-Den@DC-G16-11, demonstrated significantly lower permeability (Supplementary Fig. 3c) in the dynamic blood-brain barrier chip compared to the static transwell model[34], highlighting the advantages of the dynamic setup.

We conducted an additional assessment of the penetration capabilities of ICG-Gd-Den@DC-G16-11 within the BBB model. On the seventh day post-model construction, ICG-Gd-Den and ICG-Gd-Den@DC-G16-11 were added to the lower chamber of each model separately, and the fluorescence intensity was measured via a fluorescence spectrophotometer. After 2 h incubation, the medium was withdrawn from the upper chamber of the model, and the fluorescence intensity was measured again. The results demonstrated that both probes could efficiently penetrate the in vitro BBB model. The penetration rate of ICG-Gd-Den@DC-G16-11 was around 50%, which was notably twice as high as that of ICG-Gd-Den (Fig. 4d). As shown in Fig. 4e, the high efficiency of crossing the blood-brain barrier is related to the charge carried on the surface of the probe.The surfaces of brain capillary ECs are negatively charged under physiological pH conditions[35]. Based on this feature, one transport mechanism for macromolecules traversing the BBB is adsorptive-mediated transcytosis (AMT). This process exploits the electrostatic interactions between positively charged substrates and negatively charged ECs, resulting in the formation of vesicles for endocytosis[36], and the electrostatic interaction between positively charged probe and negatively charged blood-brain barrier facilitates the crossing of the blood–brain barrier[37]. Therefore, we hypothesized that ICG-Gd-Den@DC-G16-11 possessing a remarkably higher positive charge compared to ICG-Gd-Den, could exhibit a high efficiency to traverse the BBB.

Dual-modal probe specifically targeted GCN5-overexpressed GBM cells in vitro

To verify the specificity of ICG-Gd-Den@DC-G16-11 binding to GBM with GCN5 overexpression via its DC-G16-11 ligand, we co-cultured the probe with the GBM cell line U87, which overexpresses GCN5, and the low-grade glioma cell line CHG5, which has low GCN5 expression, for 2 h[25]. We also designed two control groups, including an ICG-Gd-Den treated group and a pre-blocking group of DC-G16-11(10 µg mL^{-1})[26] inhibitor + ICG-Gd-Den@DC-G16-11. The results showed that the ICG-Gd-Den@DC-G16-11 probe was efficiently taken up by GCN5-overexpressing U87 cells and had a fluorescence intensity ~3.6-fold greater than the low-grade glioma cell line CHG5 (Fig. 5a-b). Additionally, the signal of the ICG-Gd-Den@DC-G16-11 treated group was significantly higher than that of the ICG-Gd-Den treated group and the DC-G16-11 pre-blocking group. Therefore, these results elucidated that the ICG-Gd-Den@DC-G16-11 probe specifically targeted GCN5-overexpressed GBM cells. Subsequently, we co-cultured the U87 cell line with ICG-Gd-Den@DC-G16-11 and ICG-Gd-Den for 2 hours separately, both containing the same concentration of 150 µg mL^{-1} probes, with PBS as a blank reference. The MRI image exhibited that the probe specifically bound to GCN5-overexpressing U87 cells via a 3 T MRI system (Fig. 5c). Furthermore, the probe intracellular efficiency was quantified by evaluating the intracellular gadolinium content via an inductively coupled plasma optical emission spectrometry (ICP-OES). The cellular uptake of the ICG-Gd-Den@DC-G16-11 (40.04 ± 6.28 pg $cell^{-1}$) was significantly higher than that of the ICG-Gd-Den (25.03 ± 2.46 pg $cell^{-1}$, Fig. 5d). These results revealed the targeting specificity and cellular uptake of ICG-Gd-Den@DC-G16-11 for further in vivo imaging.

Dual-modal probe precisely delineate the borders of orthotopic GBMs via MRI

GCN5 is primarily expressed in the cytoplasm, where the positively charged probes on its surface are attracted to the negatively charged membranes of tumor cells. Upon entry into the cells, these probes bind to the target protein GCN5, probes that failed to bind to intracellular target proteins are cleared more quickly (Fig. 6a). The probes successfully penetrate the BBB and localize within the brain tumor site via the enhanced permeability and retention (EPR) effect and receptor-mediated transcytosis (RMT). To further validate the efficacy of dual-modal probes utilizing MRI for accurately delineating the boundaries of GBM, we established the orthotopic GBM mice. To closely mimic the growth characteristics of GBM seen in human patients, particularly its high invasiveness, we selected the invasive GL261 GBM model for construction[38]. Additionally, the conventional U87 GBM model was established to determine whether the nanoparticles yield consistent results across multiple GBM models. Each model was divided into three groups ($n = 3$ mice each group): ICG-Gd-Den was set as the control group, ICG-Gd-Den@DC-G16-11 as the targeting group, and

https://doi.org/10.1038/s41467-025-57598-9

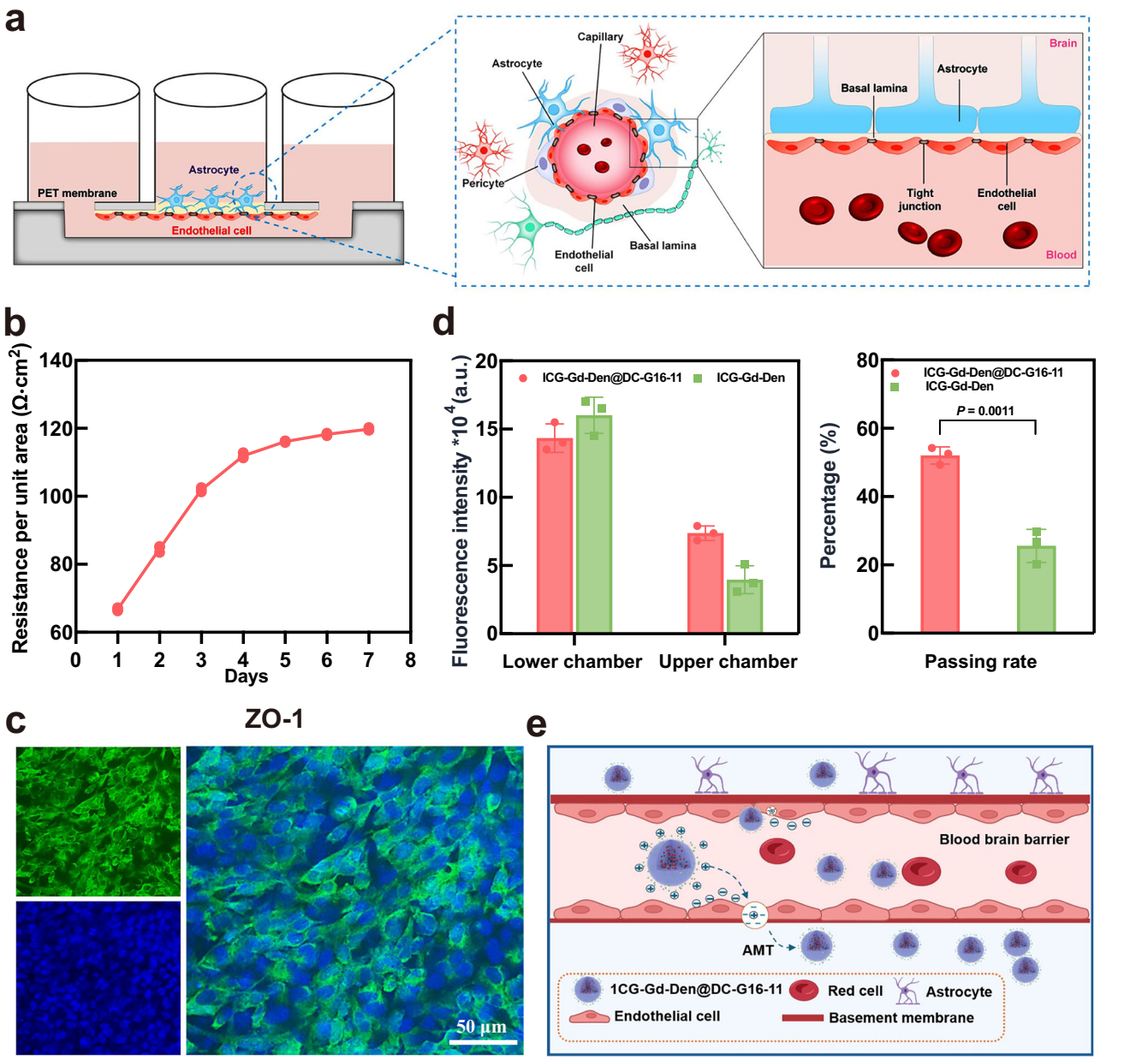

Fig. 4 | BBB-crossing ability of ICG-Gd-Den@DC-G16-11 in vitro. a Illustration of the chip design, which includes a medium-storage layer, an upper chamber for cell seeding, a PET membrane separating the upper and lower layers, and a lower chamber for cell seeding. **b** TEER measurement of the BBB model fabricated using microfluidic chips. **c** Immunofluorescence staining for the expression of the tight junction protein ZO-1. Blue: nuclei stained with DAPI; green: FITC-labeled ZO-1(Secondary antibody). **d** Quantification of fluorescence intensity in the upper and lower chambers of the BBB model for ICG-Gd-Den@DC-G16-11 and ICG-Gd-Den probes, and statistical analysis of the penetration rate of ICG-Gd-Den@DC-G16-11 and ICG-Gd-Den probes in the microfluidic chip BBB model. **e** Schematic illustration of the modes of transport for probes across the blood-brain barrier. Data in (**d**) are presented as mean values ± SD. The *p* value in (**d**) were determined by unpaired two-tailed Student's *t*-test. $^{**}p < 0.01$.

another competitive group which was first injected with a DC-G16-11 inhibitor to pre-block the binding site followed by injection of the ICG-Gd-Den@DC-G16-11. Before injection, the boundaries between the tumor tissue and surrounding brain tissue were indistinct (Fig. 6b, 0 h and Supplementary Fig. 4a, 0 h). However, after the probes injection, the tumor site, especially the peripheral regions, became markedly prominent and differentiated from the surrounding tissue (Figs. 6b, 1–8 h and Supplementary Fig. 4a, 1–8 h). The targeted group (ICG-Gd-Den@DC-G16-11) showed significantly higher MRI signal enhancement compared to the control group (ICG-Gd-Den) and the competitive group (DC-G16-11 blocked + ICG-Gd-Den@DC-G16-11). As time elapsed following the injection, the signal enhancement intensified and reached its climax at 3 h post- injection, after which minimal signal variation was observed (Fig. 6c and Supplementary Fig. 4b). These results indicated that the ICG-Gd-Den@DC-G16-11 probe has excellent MRI capabilities, provided a favorable time window for the MRI of the tumor site.

At 3 h after injection with ICG-Gd-Den@DC-G16-11, we extracted brain slices from orthotopic GBM mice model. Based on the fluorescence imaging characteristics of the dual-modal probes, we performed GCN5 fluorescence staining on the brain slices. The immunofluorescence images revealed significant co-localization of the probe (red) with GCN5 (green) (Fig. 6d and Supplementary Fig. 4c). ImageJ software analysis of brain slices from the ICG-Gd-Den, ICG-Gd-

https://doi.org/10.1038/s41467-025-57598-9

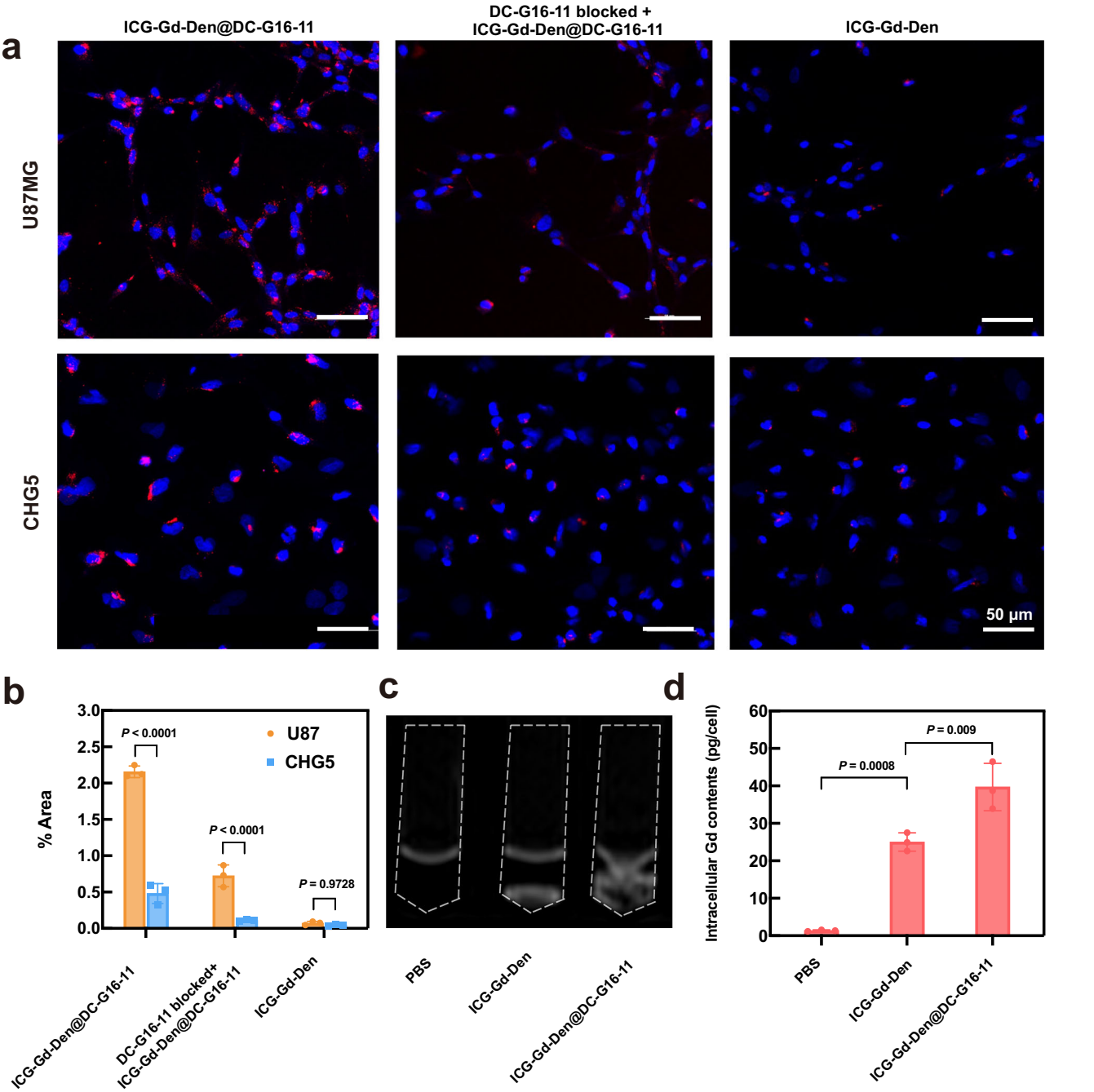

Fig. 5 | Dual-modal probe specifically targeted GCN5-overexpressed GBM cells in vitro. a CLSM images of U87 and CHG5 cells after 2-hour co-culture with ICG-Gd-Den, ICG-Gd-Den@DC-G16-11, and DC-G16-11 Blocked+ICG-Gd-Den@DC-G16-11. Blue: nuclei stained with DAPI; red: ICG encapsulated in the probe. **b** Quantitative analysis of fluorescence intensity of (**a**), $n = 3$ independent experimental replicates. **c** T1-weighted MRI images of U87 cells labeled with probes from different groups. White: T1-weighted MRI signal. **d** ICP-OES measurement of intracellular Gd content in (**c**), $n = 3$ independent experimental replicates. Data in (**b, d**) are presented as mean values ± SD. The *P* values in (**b**) was calculated by two-way ANOVA and multiple-comparison test, the *P* values in (**d**) was calculated by one-way ANOVA and multiple-comparison test. $^{**}p < 0.01$, $^{****}p < 0.0001$.

Den@DC-G16-11, and competitive group showed that the ICG-Gd-Den@DC-G16-11 probe was better able to bind to GCN5 in tumor cells than the ICG-Gd-Den, which showed no apparent signals. In the GL261 GBM model, the experimental group exhibited a fluorescence intensity that was ~ 4.7-fold higher than that of the competitive group (Fig. 6e). Similarly, in the U87 GBM model, the experimental group exhibited a fluorescence intensity that was ~ 2.7-fold higher than that of the competitive group (Supplementary Fig. 4d). The results demonstrate that dual-modal nanoprobes carrying DC-G16-11 and modified with PEG can effectively penetrate the BBB in vivo and specifically bind to GCN5 in GBM cells for MRI imaging, while remaining non-binding to normal brain cells.

Dual-modal probes displayed the borders of orthotopic GBM via fluorescence imaging

We further investigated the targeted fluorescence imaging performance of the ICG-Gd-Den@DC-G16-11 in orthotopic GBM mice via small-animal fluorescence imaging. The mice were injected intravenously with ICG-Gd-Den, ICG-Gd-Den@DC-G16-11, and the competitive group of ICG-Gd-Den@DC-G16-11 plus free DC-G16-11 inhibitor, small-

https://doi.org/10.1038/s41467-025-57598-9

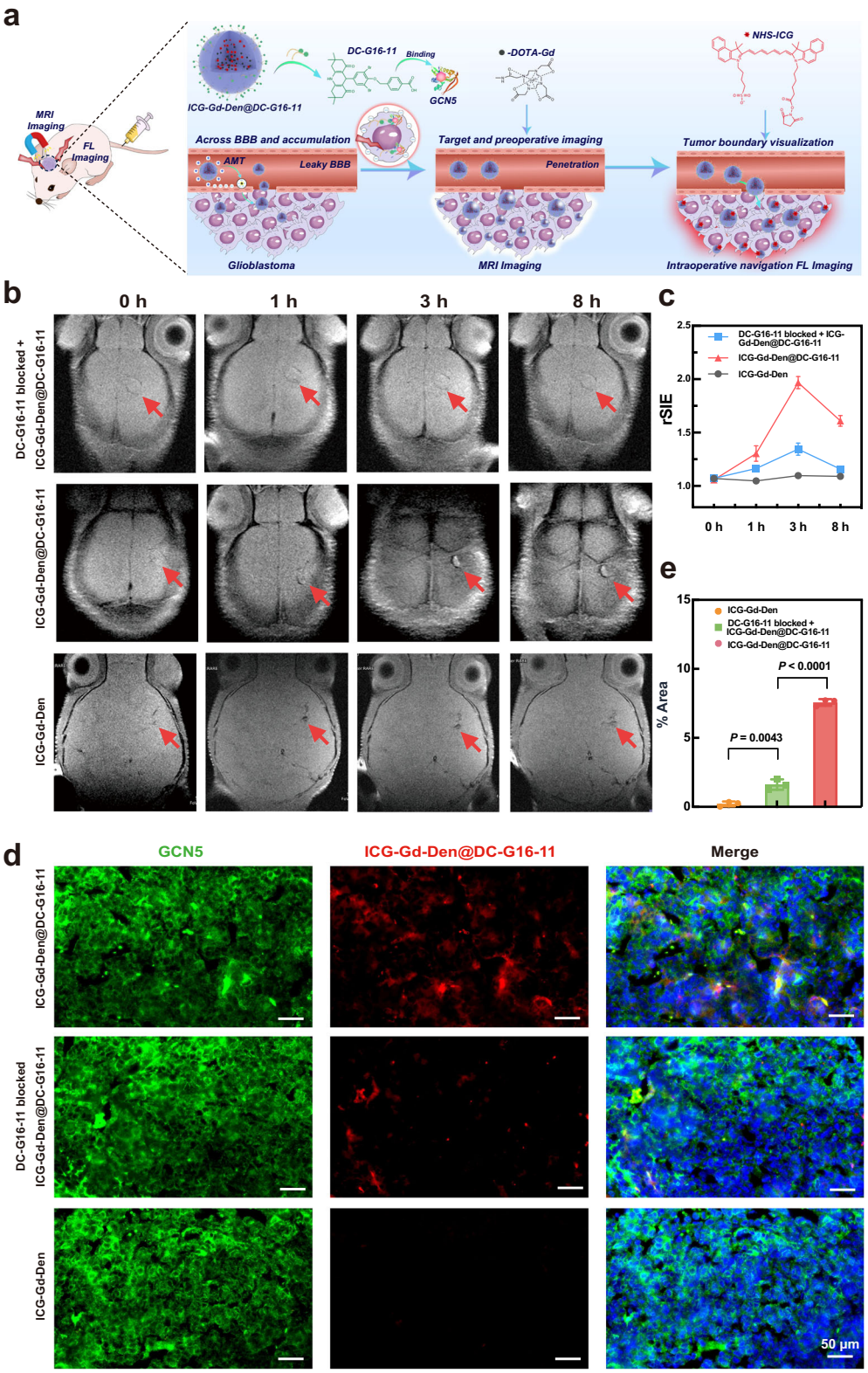

Fig. 6 | Dual-modal probe precisely delineated the borders of orthotopic GBM via MRI. a Mechanism of dual-modal imaging achieved by ICG-Gd-Den@DC-G16-11 crossing the BBB of the GBM. **b** T1-weighted magnetic resonance images on GL261 GBM mice of ICG-Gd-Den group, ICG-Gd-Den@DC-G16-11 group, and competitive group (Red arrow: tumor; white: T1-weighted MRI signal). **c** Quantification of the rSIE value in MRI images of (**b**), $n = 3$ mice per group. **d** Immunofluorescence staining of GCN5 in GL261 GBM mice brain slices and colocalization images under laser confocal microscopy (3 h after probe injection in each group). Blue: nuclei stained with DAPI; red: ICG encapsulated in the probe; green: GCN5 labeled with FITC (secondary antibody). **e** Quantification of image fluorescence intensity in (**d**), $n = 3$ independent experimental replicates. Data in (**c**, **e**) are presented as mean values ± SD. The *P* value in (**e**) was calculated by one-way ANOVA and multiple-comparison test. $^{**}p < 0.01$, $^{****}p < 0.0001$.

animal fluorescence imaging was performed at different time points. Figure 7a exhibited that the ICG-Gd-Den@DC-G16-11 probe specifically accumulated in the tumor site of orthotopic GL261 GBM mice. The fluorescence signals in the tumor site of the competitive-group mice were observably weaker than those in the ICG-Gd-Den@DC-G16-11 group. In contrast, no detectable fluorescence signal was observed in the control group. These results revealed the tumor specific targeting ability of ICG-Gd-Den@DC-G16-11. Different fluorescent signals in the tumor site suggest the specific accumulation of the tumor targeted by DC-G16-11.

Subsequently, the treated orthotopic GL261 GBM mice were sacrificed, and the fluorescence intensity of main organs including heart, lungs, intestines, stomach, liver, spleen, kidneys, and brain were measured. According to the fluorescence intensity of main organs (Fig. 7b, c), the probes were mainly metabolized and eliminated from the body through the kidneys. Only a small amount of the probes accumulated in the liver, stomach, and lungs. These results indicated low expression of GCN5 in these organs and the probes were partly captured by the reticuloendothelial system (RES)[39]. To clarify the dependence of fluorescence intensity in tumors at different time points, we measured the fluorescence intensity in tumor site confirming that it significantly increased and culminated at 3 hours post-injection (Supplementary Fig. 5), which is consistent with the observation in the MRI study. The fluorescence intensity of ICG-Gd-Den@DC-G16-11 probe was 2.1 times higher than the competitive group in tumor site, indicating the DC-G16-11 conjugation improved the target efficiency of the probes. Subsequently, the in vivo hemodynamic data showed that the blood concentration levels of the ICG-Gd-Den and ICG-Gd-Den@DC-G16-11 probes significantly decreased with time and remained approximately 8% ID g^{-1} at 6 h after injection (Fig. 7d). By applying a two-compartment model[40], the blood-clearance half-lives of the ICG-Gd-Den and ICG-Gd-Den@DC-G16-11 probes were determined to be 72.5 and 84.5 min, respectively. These values are comparable to the blood half-lives of currently used commercial MRI contrast agents[41], indicating that our dual-modal probe can ensure imaging clarity and quality while evading RES uptake and undesired accumulation in non-targeted organs of the body.

After fluorescence imaging, tissue sections of treated mice were stained with H&E and imaged using confocal microscopy. H&E staining of brain sections revealed that the orthotopic GL261 GBM model exhibited notable aggressiveness, characterized by the infiltrative growth of the tumor into normal brain tissue. The tumor cells exhibited deep-staining nuclei, pronounced nuclear atypia, uneven chromatin distribution, and enlarged nucleoli, along with evident angiogenesis within the tumor (Fig. 7e). In contrast, the invasiveness observed in the U87 GBM model was less pronounced (Supplementary Fig. 4e). The probes were able to accurately delineate the tumor boundary in both orthotopic GBM models, indicating the notable diagnostic efficiency. Under confocal microscopy, we observed significant uptake of ICG-Gd-Den@DC-G16-11 probes in the cytoplasm of tumor cells within the fluorescent slices, whereas normal brain cells, as indicated by HE-stained control images, showed no noticeable uptake of the probe (Fig. 7f and Supplementary Fig. 4e). Similarly, a certain amount of ICG-Gd-Den@DC-G16-11 probe were also accumulated in the brain slices of the competitive group, which is consistent with the images obtained from small animal fluorescence imaging (Supplementary Fig. 6a, b). This phenomenon is hypothesized to attributed to the limited ability of DC-G16-11 to penetrate the BBB, thereby preventing it from fully occupying the GCN5 binding sites. In contrast, a certain amount of ICG-Gd-Den@DC-G16-11 can still cross the BBB and bind to GCN5 for imaging.

To validate the ability of ICG-DEN@DC-G16-11 to display tumor boundaries during surgery, orthotopic GL261 GBM mice were treated with the probe and underwent real-time fluorescence imaging using a clinical-grade intraoperative fluorescence imaging platform. For better exposure, the entire brain was removed and exposed to the irradiation of intraoperative navigation device. The tumor site emitting distinct green fluorescence signal was displayed using the accompanying near-infrared fluorescence imaging system (Supplementary Fig. 7a), confirming that ICG-DEN@DC-G16-11 can clearly display tumor boundaries through full-course real-time near-infrared fluorescence imaging. Subsequent H&E staining of brain slices showed that the tumor outline was consistent with the intraoperative navigation images of the GL261 model (Supplementary Fig. 7b, left). Moreover, CLSM images of the brain showed that tumor cells infiltrating the brain parenchyma at the edges contained ICG-DEN@DC-G16-11, exhibiting distinct red fluorescence (Supplementary Fig. 7b, right).

To further evaluate the sensitivity of ICG-DEN@DC-G16-11 to early-stage GBM, we also used a small tumor foci model at an early stage of the orthotopic GL261 GBM mice. On the seventh day following transplantation, intraoperative navigation imaging revealed a faint fluorescent signal in the left hemisphere of the brain (Supplementary Fig. 7c). Upon bisecting the mouse brain along the midline, the small tumor foci in the left hemisphere exhibited a clear fluorescent signal with a well-defined outline (Supplementary Fig. 7d). This result indicated that the sensitivity of ICG-DEN@DC-G16-11 is sufficient for imaging with intraoperative navigation equipment, and the brain tumor-targeting efficiency of ICG-DEN@DC-G16-11 was highly reliable. In summary, our dual-modal probe specifically accumulated in the GCN5 high-expression GBM area, providing the possibility for accurately determining surgical margins using NIR imaging.

Discussion

In this study, we develop a dual-modal probe for magnetic resonance and fluorescence imaging, capable of targeting elevated GCN5 expression levels in GBM to enhance the precise delineation of tumor boundaries. This probe exhibited its high efficiency for surgical resection guiding, thereby reducing the probability of recurrence. The study started with the differential expression genes between glioma and normal brain tissue, exploring the potential of GCN5 targeting in glioblastoma detection, including using GCN5 targeting to determine surgical margins. Through comprehensive multi-omics analysis of big data and mechanistic research, we confirmed the correlation of GCN5 with glioma grading, showing significantly upregulated expression levels in GBM and being unexpressed in normal brain tissue. Our results suggest that GCN5 may contribute to the malignant progression of glioma, and utilizing GCN5 as a target to construct probes holds potential for delineating GBM boundaries precisely.

The existence of the BBB blocks over 98% of therapeutic agents from entering the brain[42]. Therefore, increasing the permeability of drugs across the BBB is recognized as the first and most crucial step for glioma treatment. Facilitating the transport of molecular drugs across the BBB for precise delineation of GBM remains a significant challenge. Our study indicates that the dual-modal probe, which effectively targets GCN5 in GBM, may offer substantial advancements. Previous studies have shown that nanoparticles with a diameter of 20-50 nm are taken up by mammalian cells at a faster and higher rate and concentration compared to other sizes and shapes[43]. In the systemic physiological environment, the glycocalyx, consisting of the sialo-glycoconjugates and heparan sulfate proteoglycans expressed on the luminal surface of BCECs, contributes to an overall negative charge of BBB[44,45]. Therefore, cationized nanodrugs could trigger the adsorption-mediated endocytosis, i.e., AMT based drug delivery, by electrostatic interactions between the positively charged moieties of the nanodrugs and the negatively charged membrane surface regions of the BBB[46]. The maximal binding capacity (Bmax) of AMT is several thousand times higher than that of RMT, leading to significantly higher transcellular transport[45]. Additionally, positively charged probes are more likely to adsorb onto negatively charged cell membranes and be engulfed by cells, thereby gaining the opportunity to interact with proteins within the cytoplasm[2,47,48]. Due to the method of crossing the blood-brain

https://doi.org/10.1038/s41467-025-57598-9

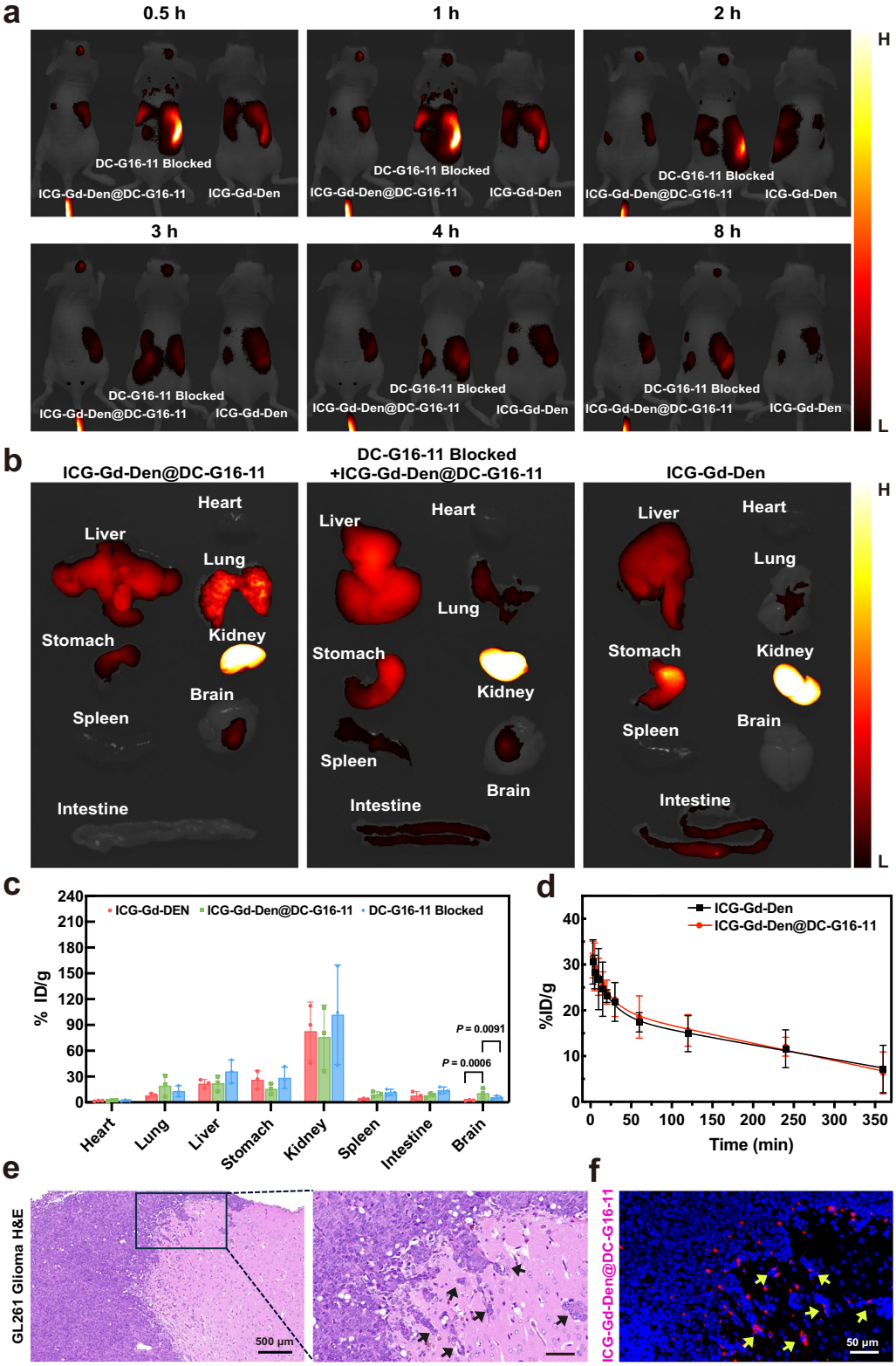

Fig. 7 | Dual-modal probe displayed the borders of orthotopic GBM via fluorescence imaging. a Fluorescence images of orthotopic GL261 GBM mice injected with ICG-Gd-Den, ICG-Gd-Den@DC-G16-11, and DC-G16-11 Blocked+ICG-Gd-Den@DC-G16-11 at different time points ($n = 3$ mice each group). **b** Ex vivo fluorescence imaging of main organs from mice in (**a**). **c** Fluorescence quantification of (**b**), $n = 3$ independent experimental replicates. **d** Blood-clearance efficiency of the ICG-Gd-Den and ICG-Gd-Den@DC-G16-11 probes after intravenous injection ($n = 3$ independent experimental replicates). **e** H&E staining of brain slices in the ICG-Gd-Den@DC-G16-11 group, black arrows: tumor cells invading normal brain tissue. **f** CLSM images corresponding to the brain slices in (**e**). Yellow arrow: ICG-Gd-Den@DC-G16-11 bound to tumor cells; blue: nuclei stained with DAPI; red: ICG encapsulated in the probe (**e**, **f**, $n = 3$ independent experimental replicates). Data in (**c, d**) are presented as mean values ± SD. The *P* values in (**c**) was calculated by one-way ANOVA test and multiple-comparison test. $^{**}p < 0.01$, $^{***}p < 0.001$.

barrier mediated by AMT and the inherent advantages of Den nanomaterials, our improved nanoprobe demonstrated a 50% crossing rate in an in vitro BBB model. This demonstrates improved permeability of nanoprobes across the blood-brain barrier compared to previous studies[17,49]. Our results in this study also suggest that the binding of ICG-Gd-Den@DC-G16-11 and GCN5 occurred inside the cell after the probe was actively phagocytosed, and the unmodified ICG-Gd-Den is expelled from the cell more quickly after being phagocytosed by the cells.

Malignant tumors are known to disrupt the integrity of the BBB, resulting in a blood-brain tumor barrier (BTB) that exhibits significant heterogeneity and is characterized by various distinct features. In the presence of an intact BBB, hydrophobic molecules with a molecular weight of less than 500 Da and smaller than 1 nm are capable of diffusing transcellularly into the neuroparenchyma[50]. However, the downregulation of ZO-1 and vascular endothelial cell adhesion molecule (VE-CAM) in the BTB leads to a loss of continuous endothelial cell adhesion, resulting in the formation of abnormal molecular permeation pathways[51]. This leads to nanoparticles with a size of less than 20 nm being able to cross the BTB more easily[52]. In vivo fluorescence imaging experiments, we observed a notable phenomenon: larger tumors in the animal model exhibited a greater accumulation of the probe, leading to increased fluorescence intensity. Therefore, we hypothesize that the probe, with a particle size of 20 nm, can effectively traverse the highly permeable BTB, rather than relying exclusively on active targeting mechanisms.

Our research confirms the significance of GCN5 as a diagnostic target for GBM. The dual-modal probe designed in this study can assist surgeons in achieving a precise diagnosis via MRI before surgery. During surgery, fluorescence imaging can be performed for visual detection, providing differentiation between the tumor's borders and the surrounding normal tissue. Considering the limited effectiveness of current GCN5 small molecule inhibitors in tumor suppression[53], the prospects for drug development targeting GCN5 remain uncertain at this time. However, by utilizing the precise targeting capabilities of GCN5 for accurate localization of GBM, we plan to focus on future research aimed at developing nanotechnology-based drug delivery systems. This approach aims to investigate the potential of targeting GCN5 in combination with first-line drugs such as temozolomide, carmustine, or bevacizumab[54], which may enhance therapeutic efficacy against GBM by improving the efficiency of drug delivery to the tumor.

Methods

Ethical statement

This research complies with all relevant ethical regulations. All surgical interventions carried out and the subsequent postoperative care provided to the animals have been reviewed and approved by the Animal Protection and Use Committee of Shanghai Jiao Tong University School of Medicine Affiliated Ninth People's Hospital, China, with protocol number SH9H-2019-A710-1. Sex was not considered in the study design because this variable was not relevant to the study, and female mice were selected in this study to ensure gender uniformity. 87 human GBM tissue samples were collected from the Ninth People's Hospital of Shanghai Jiao Tong University School of Medicine. Sex was not considered in the study design. The study was approved by the Ethics Committee of the Ninth People's Hospital of Shanghai Jiao Tong University School of Medicine, China (Protocol No.: SH9H-2024-T499-1), all participants provided written informed consent and were not compensated.

Materials

NHS-PEG-DC-G16-11 was custom-made from Suzhou Qiangyao Biotechnology Co., Ltd (Suzhou, China) according to the chemical structure reported in the literature[26]. PAMAM G2-NH2 dendrimers (Den) was purchased from XINQBio Co., Ltd (Hangzhou, China). Gadolinium chloride ($GdCl_3$) and indocyanine green (ICG) were purchased from Energy Chemical. N-hydroxy succinimide (NHS), DOTA-NHS, fluorescein-carboxylic acid (FITC-COOH), polyethylene glycol (PEG) and 1-Ethyl-3-(3-dimethylaminopropyl) carbodiimide (EDC) were purchased from Aladdin. Dimethyl sulfoxide (DMSO) was purchased from yuanye Biotechnology Co., Ltd (Shanghai, China). 4',6-diamidino-2-phenylindole (DAPI), 4-(2-hydroxyethyl)-1-piperazineethanesulfonic acid (HEPES), Dulbecco's Modified Eagle Medium (DMEM) and fetal bovine serum (FBS) were purchased from Thermo Fisher Scientific. MTT Cell Proliferation and Cytotoxicity Assay Kit, protease inhibitors, 6X loading buffer were purchased from Beyotime Biotechnology Co., Ltd (Shanghai, china). Microfluidic chip was purchased from Daxiangbio Co., Ltd (Beijing, China). The fusion plasmid GCN5-GFP was purchased from Shanghai Genechem Co., Ltd. (Shanghai, China). Anti-KAT2A/GCN5 Antibody (abcm, clone name: AT3G13, Catalog number: ab208907, Lot Number: 1003062-3; 1:300 dilution); antibodies against GCN5 (Santa cruz, clone name: A-11, Catalog number: sc-365321; Lot Number: F0822; 1:300 dilution); rabbit anti-TJP1 antibody (Anti-ZO-1 antibody) (Sino Biological, Catalog number: 102305-T02, 1:500 dilution); goat polyclonal secondary antibody to mouse IgG (H + L) labeled with Alexa Fluor 488 (Abcam; Catalog number: ab150113; 1:500 dilution); FITC-labeled goat anti-rabbit IgG (Beyotime, Catalog number: A0562,1:500 dilution); mouse GFP(1:1000; abcam ab291); mouse ACTIN (1:10000; abcam ab6276).

Clinical samples

We collected 87 formalin-fixed, paraffin-embedded (FFPE) GBM tissue samples from Shanghai Ninth People's Hospital, Shanghai Jiao Tong University School of Medicine. Histopathological and immunohistochemical diagnoses were performed independently by two neuropathology experts following the 2016 World Health Organization (WHO) classification of central nervous system tumors. Informed consent was obtained from all patients prior to sample collection, in accordance with the ethical guidelines of the Ethics Committee of the Ninth People's Hospital of Shanghai Jiao Tong University School of Medicine, China. The clinical and pathological characteristics of the 87 glioma cases are summarized in Supplementary Table 1.

Cell culture

The human GBM cells U87 (Catalog No. BNCC338150), U251 (Catalog No.BNCC101001), H4 (Catalog No. BNCC101682), A172 (Catalog No. BNCC341782), LN229 (Catalog No. BNCC341218) and human microglia cells HMC3 (Catalog No. BNCC342264) were obtained from the Beijing BeNa Culture Collection (Beijing, China). Additionally, the low-grade glioma cells CHG5, the GBM cell lines GL261 and TJ905 were generously provided by Dr. X.B. from the Third Military Medical University. The human brain microvascular endothelial cells hCMEC/D3, astrocytes HA-1800, and human brain astrocyte HEB was donated by D.L. from Huaqiao University. All cell lines were authenticated by STR analysis and routinely tested to be free of mycoplasma. Cells were cultured in DMEM supplemented with 10% FBS and maintained in a humidified incubator at 37 °C with 5% CO_2. And the cells for all experiments were in logarithmic growth phase.

Plasmid construction and transfection

For transient overexpression, TJ905 cells were transfected with the plasmid using Lipofectamine 3000 (Invitrogen) following the manufacturer's instructions. Cells were plated, transfected with DNA-Lipo3000 complexes, and incubated at 37 °C with 5% CO_2. After 24-48 hours, cells were lysed for mRNA and protein level validation or used for downstream experiments.

Immunoblotting

Immunoblotting was performed according to standard protocols. In short, cells were lysed in lysis buffer (Invitrogen) supplemented with protease inhibitors and kept on ice for 15 min. After centrifugation,

proteins were quantified using the BCA protein assay kit (Solarbio) and mixed with 6X loading buffer. Samples were boiled for 10 min and subjected to SDS–PAGE, followed by transferring onto PVDF membranes (Millipore). Membranes were incubated with primary antibodies overnight at 4 °C, and then with HRP-conjugated species-specific antibodies (Beyotime, 1:1000) at room temperature for half an hour. The following primary antibodies were used: mouse GCN5 (1:300; abcam ab208097), mouse GFP (1:1000; abcam ab291), mouse ACTIN (1:10000; abcam ab6276).

Colony formation assay

U87 Cas9 and GCN5-KO cells, as well as TJ905 cells transfected with either GFP or GCN5, were seeded at an appropriate density in six-well plates. The cells were cultured for over 14 days until visible colonies formed. Colonies were then fixed with absolute ethanol and stained with 0.5% crystal violet. After washing with PBS, the plates were air-dried before imaging and quantification. Colony numbers were counted and statistically analyzed.

Immunofluorescence analysis

Cells were washed twice with DPBS, fixed with 4% paraformaldehyde for 15 min, and permeabilized with 0.25% Triton X-100 for 10 min. After incubation in a blocking buffer for 45 min, the cells were incubated overnight at 4 °C with the following primary antibodies: anti-GCN5 (abcam ab208097, 1:200 dilution). Then, they were incubated with the Alexa Fluor secondary antibody (abcam, ab150113) for 1 h at room temperature. A mounting medium containing DAPI was used for counterstaining.

Construction of dual-modal probe

To synthesize the Den-Gd-DC-G16 probes, 50 μL of hydrochloric acid solution containing concentrated gadolinium chloride (50 mg mL^{-1}) was mixed with 1 mg of NHS-DOTA. The pH was adjusted to 6 using 0.25 M sodium carbonate solution, and the mixture was heated to 60°C for 30 min. Next, 1 mL of HEPES buffer containing 20 mg mL^{-1} of Den was added. Subsequently, 20 mg of Den-Gd was mixed with 1 mg of NHS-PEG-DC-G16-11 in HEPES buffer (pH 8.4) and stirred for 1 h. The product was dialyzed in ultrapure water (7000 Da membrane) to remove unreacted components. The purified probes were designated as Den-Gd-DC-G16. Then, NHS-ICG was added to the solution and stirred at room temperature for 4 h. The resulting ICG-Gd-Den@DC-G16-11 was isolated by centrifugation and further purified by dialysis to remove unreacted NHS-ICG.

Physical characterization of the probes

Surface morphology was analyzed using STEM with a JEOL JEM-2100 instrument. A 10 μL sample of the probe was placed on a copper grid, air-dried, and stained with 1.5% phosphotungstic acid (pH 6.0) for 10 min before STEM imaging and mapping. Gadolinium concentration on the probe surface was measured by ICP-OES with a Thermo Scientific iCAP-6300 spectrometer. Hydrated particle size and surface potential were determined at each coupling step using a Malvern Zetasizer (Malvern Panalytical, UK). Probe samples, surface-grafted with ICG at varying concentrations of Gd ions (0, 15, 30, 70, and 150 μg mL^{-1}), were analyzed for fluorescence intensity using a VISQUE InVivo Smart NIR fluorescence-imaging system and a Siemens 3 T Trio MRI system with a clinical head-imaging coil, respectively. Gadolinium-ion loading capacity and in vitro stability under physiological conditions (PBS and serum) were also evaluated. Particle size and fluorescence intensity were monitored at different incubation times (0, 6, 12, 24, 32, 48 h). Longitudinal relaxation time (T_1) was measured with a Bruker MQ60 relaxation analyzer at 37 °C and 1.4 T (60 MHz). The magnetization recovery curve was used to assess T_1, and gadolinium concentration (s^{-1}) was calculated by fitting the inverted relaxation time ($1/T_1$) and determining the T_1 relaxivity (r_1) according to a standard formula.

Verification of the probe's GCN5 targeted efficacy

The activator is prepared by mixing 400 mM EDC and 100 mM NHS immediately prior to injection. The CM5 sensor chip (cytiva) is activated for 420 s with the mixture at a flow rate of 10 μL min^{-1}. Dilute GCN5 to 20 μg mL^{-1} in immobilization buffer, then injected it into sample channel Fc2 at a flow rate of 10 μL min^{-1}, and typically result in immobilization levels of 12600 RU, the reference channel Fc1 does not need a ligand immobilization step. The chip is deactivated by 1 M Ethanolamine hydrochloride at a flow rate of 10 μL min^{-1} for 420 s. Dilute ICG-Gd-Den@DC-G16-11 with the same analyte buffer to 8 concentrations (0.16-10) μM. ICG-Gd-Den@DC-G16-11 is injected to channel Fc1- Fc2 at a flow rate of 20 mL min^{-1} for an association phase of 100 s, followed by 180 s dissociation. The association and dissociation processes are all handlled in the analyte buffer. Repeat 8 cycles of analyte according to analyte concentrations in ascending order. After each cycle of interaction analysis, the chip needs to be regenerated.

Construction of BBB chip model

A microfluidic chip (Daxiangbio, Beijing, China) was prepared by rendering the channels hydrophilic with PBS under dynamic conditions ((2 cycles per min, 30 degrees shaking angle) at 37°C). The channels were coated with 0.3 mg mL^{-1} mouse-tail collagen (Corning) and incubated for 2 h. HA-1800 cells (2.5×10^6 cells mL^{-1}) were seeded into the upper chamber, allowed to adhere for 2 h, and cultured dynamically for 2 days in DMEM with daily medium refresh. Human cerebral microvascular endothelial cells (hCMEC/D3, 1×10^7 cells mL^{-1}) were then seeded into the lower chamber, allowed to attach statically for 2 h, and cultured dynamically. The transepithelial electric resistance (TEER) was monitored every day using an epithelial voltohmmeter (Millicell-RES, Millipore, USA). The tight junctions of the in vitro model could be regarded to mimic the real BBB when the TEER values reached a stable level. The tight junction formation of the BBB model was confirmed by ZO-1 (Sino Biological, 1:500 dilution in PBS) immunofluorescence staining, performed after fixation and blocking, followed by imaging with an inverted fluorescence microscope (Olympus IX73, Tokyo, Japan).

Permeability of tracer dyes to validate BBB model

The permeability of the compound was determined by measuring its diffusion rate across the membrane. A 200 μL solution of fluorescein sodium (FLU) at a concentration of 0.05 mg mL^{-1} and a 1.25 mg mL^{-1} solution of FITC-dextran (40 kDa, 70 kDa) were added to the vascular compartment of the chip, while 100 μL of culture medium was added to the neural compartment. After 2 hours, samples were taken from the neural compartment, diluted two-fold with culture medium, and the fluorescence intensity of the samples was measured using a fluorescence spectrophotometer. The permeability coefficient was calculated using Artursson's (1990) coefficient formula:

$$P_{app}(cms^{-1}) = \frac{dQ}{dt} \times \frac{1}{A} \times \frac{1}{C_0} \quad (1)$$

$\frac{dQ}{dt}$ represents the amount of a measured substance passing through per second; $\frac{1}{A}$ represents the reciprocal of the membrane surface area; $\frac{1}{C_0}$ represents the reciprocal of the initial concentration of the substance being measured.

Measurement of BBB permeability of probe in vitro

To evaluate BBB penetration, 200 μL of ICG-Gd-Den@DC-G16-11 (150 μg mL^{-1}) was introduced into the vascular chamber of the chip, while 100 μL of medium was added to the neural chamber. After a 2-hour incubation, the solution from the neural chamber was collected, diluted 1:2 with medium, and its fluorescence intensity measured using a fluorospectrometer (NanoDrop 3300, Thermo Fisher Scientific, MA, USA). BBB penetration efficiency was calculated as the fluorescence intensity ratio between the neural and vascular chambers.

In vitro visualization of the probe via MRI

U87 cells with a wall attachment rate exceeding 80% were prepared in six-well plates by aspirating the culture medium. A mixture of ICG-Gd-Den@DC-G16-11, ICG-Gd-Den probes, and serum-free DMEM was added at Gd concentrations of 150 μg mL^{-1}, followed by incubation in a 37°C, 5% CO_2 culture chamber for 2 hours. Afterward, the cells were detached using trypsin, collected in 5 mL centrifuge tubes with 3 mL PBS, and dispersed evenly. Approximately 5×10^5 cells were transferred into 2 mL centrifuge tubes, centrifuged to remove the supernatant, and resuspended in 300 μL of 2% (w/v) gelatin solution (BioLeaf, Shanghai, China). The mixture was solidified on ice for 30 minutes. Control group was prepared using PBS at the same time. T1 imaging was performed using a Siemens 3 T Trio MRI system with a clinical head-imaging coil. Imaging parameters included a slice thickness of 2.3 mm, TE = 7.8 ms, TR = 500 ms, and FOV = 60 × 60 mm. The T1 relaxation time for the region of interest was calculated from the acquired data.

Evaluation of probe phagocytosis by cells in vitro

Cell samples prepared for MRI imaging were thawed at room temperature, and the PBS-gelatin mixture was centrifuged to remove the supernatant. Subsequently, 1 mL of concentrated nitric acid was added to the pellet, and the sample was incubated at 37 °C for 24–48 h in a constant-temperature incubator until complete digestion of the cells. The digested solution was then diluted to a final volume of 10 mL, and the gadolinium concentration was measured using ICP-OES, with results expressed in mg mL^{-1}. The calculation method for the gadolinium content in a single cell, W_{Gd} is:

$$W_{Gd} = \frac{C_{Gd}}{n}. \quad (2)$$

where as C_{Gd} is the total concentration of Gd atoms, and n is quantified cell number.

Quantitative detection of probe phagocytosis by cells in vitro

U87 cells and CHG5 glioma cells (1×10^5 cells) were seeded in 3.5 cm confocal dishes to evaluate the cellular uptake of the ICG-Gd-Den@DC-G16-11 probe. Once the cells reached approximately 80% confluency, they were incubated with one of three nanoparticle samples at a concentration of 150 μg mL^{-1}: ICG-Gd-Den@DC-G16-11, ICG-Gd-Den@DC-G16-11 with excess competitive DC-G16-11 inhibitor, or ICG-Gd-Den. The incubation was carried out at 37 °C for 2 h. Afterward, the cells were washed three times with PBS, stained with 500 μL of DAPI dye, and incubated at 37 °C for 15 min. Finally, cellular uptake was visualized and analyzed using a confocal scanning laser microscope (OLYMPUS FV4000, DAPI: 405 nm, ICG: 785 nm).

Biocompatibility evaluation of the probe in vitro

The cytotoxicity of the ICG-Gd-Den@DC-G16-11 probe was assessed using the MTT assay. U87, HEB, and CHG5 cells were seeded in 96-well plates at a density of 1×10^4 cells per well. Cells were treated with PBS (control group) or the probes at a concentration of 150 μg mL^{-1} and incubated for 24 or 48 h. Following incubation, the cells were washed three times with PBS, and 100 μL of MTT solution was added to each well. After 4 h, the MTT solution was replaced with 100 μL of dimethyl sulfoxide (DMSO) to dissolve the formazan crystals. The absorbance at 490 nm was measured using a microplate reader (EnVision, Hunan, China). Cell viability was calculated as the percentage of absorbance in treated cells compared to untreated control cells.

Establishment of orthotopic GBM mice models

Six-week-old female BALB/c nude mice were purchased from SLAC Laboratory Animal Center, Shanghai, China. During the experiments, the mice were anesthetized with 5% pentobarbital sodium at a dose of 0.05 μL per 10 grams of body weight. A small hole was drilled 2 mm to the right and 0.5 mm upward from the anterior fontanelle of each mice. Using a single-arm brain stereotaxic apparatus (NeuroStar, Malvern, PA), a microinjector was inserted vertically to a depth of 3.5 mm, retracted 1 mm over 5 min, and 5×10^5 U87 cells or 1×10^5 GL261 cells suspended in 5 μL of substrate gel were injected. After a 5-min pause, the injector was slowly withdrawn. Mice with their wound sterilized and seamed were carefully housed in a specific pathogenfree (SPF) environment. Tumor size was assessed via MRI two weeks after inoculation. No tumors exceeded the maximum permissible diameter of 2 cm or 10% of the total body weight, as stipulated by the Ethics Committee. During the experiment, all animals were housed in a controlled environment maintained at a temperature of 24 °C and a humidity level of 30%–50%, following a strict light/dark cycle of 12 h each. The animals had unrestricted access to both water and food.

Blood biochemistry examinationkey

BALB/c nude mice (6–8 weeks old) were randomly assigned to three groups ($n = 3$ per group). Each group received an intravenous injection via the tail vein of either physiological saline, ICG-Gd-Den@DC-G16-11, or ICG-Gd-Den probes (100 μL of 20 mg mL^{-1}, Gd concentration: 1.5 mg mL^{-1}). Blood samples were collected through orbital bleeding 7 days after probe injection. Serum was obtained by centrifuging whole blood at 800 g for 5 min. Blood biochemistry analysis was performed using an automated chemistry analyzer (Chemray 240, Rayto Inc.) at Servicebio Technology Co., Ltd. (Wuhan, China).

In vivo visualization of the probe via MRI

To assess the specific targeting of GCN5 by the probe and its MRI effect in an orthotopic GBM mice model, we established three experimental groups: ICG-Gd-Den@DC-G16-11, ICG-Gd-Den (control), and a competitive group of ICG-Gd-Den@DC-G16-11 plus free DC-G16-11 inhibitor. In the competitive group, a DC-G16-11 inhibitor (150 μg per mice) was injected intravenously, followed by a second injection of ICG-Gd-Den@DC-G16-11 after 30 minutes. Each group underwent three parallel experiments with tail vein injections. The probes (100 μL of 20 mg mL^{-1}, Gd concentration: 1.5 mg mL^{-1}) were diluted in 100 μL saline and injected into the tail veins of anesthetized mice. MRI was performed at 0, 1, 3 and 8 h post-injection using a 7 T MRI scanner (BioSpec System 70/20, Bruker). T1-weighted images were acquired with the following parameters: TR = 400 ms, TE = 8.02 ms, slice thickness = 1.00 mm, FOV = 35 × 25 mm, matrix size = 256 × 256 mm. MRI images were analyzed using ParaVision 360 v3.1 software. The relative signal intensity enhancement (rSIE) was calculated as the ratio of the post-injection tumor intensity to the baseline intensity.

In vivo visualization of the probe via fluorescence imaging

To further assess the probe's ability to specifically target GCN5 in GBM models, small-animal fluorescence imaging (VISQUE InVivo Smart, Anyang-si, South Korea) was performed at 0.5, 1.0, 2.0, 3.0, 4.0 and 8.0 h after intravenous injection of the probes. This was done to observe probe distribution in the mice model. Following imaging, the mice were euthanized, and fluorescence distribution was evaluated in various organs, including the heart, lungs, liver, spleen, kidneys, small intestine, and brain. Organ weights were also recorded. The probe distribution in each organ was quantified using the formula: % ID g^{-1} = (organ fluorescence intensity + total fluorescence intensity) × 100%/organ mass.

Detection of the blood half-life of the probe

ICG-Gd-Den@DC-G16-11 and ICG-Gd-Den probes (100 μL of 20 mg mL^{-1}) were slowly injected into the tail veins of anesthetized mice ($n = 3$ mice). Blood samples were then collected at various time points (10, 15, 20, 30, 60, 120 and 240 min) via tail-vein puncture using a capillary tube. The blood samples were weighed, and fluorescence intensity was measured using a fluorescence spectrophotometer to generate a

time–fluorescence intensity curve. The blood half-life of the ICG-Gd-Den@DC-G16-11 probe was calculated using a two-compartment intravenous model and nonlinear regression analysis (GraphPad Prism 9, GraphPad Software).

Intraoperative navigation imaging

Three hours after the injection of the ICG-Gd-Den@DC-G16-11 (100 µL of 20 mg mL^{-1}), the mice underwent craniotomy and intraoperative navigation imaging using a clinical-grade fluorescence laryngoscope imaging platform (DPM-III-01, Zhuhai Deep Medical Technology Co., Ltd.) for real-time fluorescence imaging. All imaging procedures were performed with the same settings (808 nm, 2.4 W, exposure time: 30 ms, excitation power 20%, gain 3 dB). In order to expose the field of view more clearly, we perfused the mice heart apex with formalin injection, and then performed intraoperative navigation probe irradiation on the whole brain. With the probe irradiation using the intraoperative navigation device, the tumor area emitted green fluorescence, which was clearly observed in the accompanying image display system.

Statistics & Reproducibility

Data were presented as means ± standard deviation (SD). The results were analyzed by the paired or unpaired two-sided Student's t-test between two groups. One-way analysis of variance (ANOVA) and multiple comparison was used to determine statistical significance. Two-sided Mann-Whitney U test (Wilcoxon rank-sum test) was used to analyze the differential expression of GCN5 in different grades of gliomas. Categorical data were evaluated using the two-sided Chi-square (χ^2) test. All statistical analyses were conducted using GraphPad Prism 9 (GraphPad Software, Inc., La Jolla, CA, USA). Exact *P* values were provided accordingly in the figures or captions. For all graphs, $^{*}p < 0.05$; $^{**}p < 0.01$; $^{***}p < 0.001$; and $^{****}p < 0.0001$. No statistical method was used to predetermine sample size. The experiments were not randomized. The Investigators were not blinded to allocation during experiments and outcome assessment. The exact number of replicates and the statistical tests are employed are specified in the figure legends. Unless otherwise indicated, n represents the number of independent experimental replicates. For the data in Figs. 2b–d, 4d, 7e and Supplementary Figs. 4c, 4e, 6a, 6b, and 7b, three independent experiments were conducted, yielding equivalent results. The results from representative experiments are displayed.

Reporting summary

Further information on research design is available in the Nature Portfolio Reporting Summary linked to this article.

Data availability

The expression of GCN5 and related gene expressions, as well as clinical data analysis, were obtained from the Chinese Glioma Genome Atlas (CGGA) project (Download | CGGA - Chinese Glioma Genome Atlas). The GCN5 grading and tissue chip clinical grading violin plot visualizations were generated using Hiplot (https://hiplot.com.cn/cloud-tool/drawing-tool/detail/119). All other datadata generated or analyzed during this study are available within the article, Supplementary Information file and the Source Data file. Source data are provided with this paper.

References

1. Stupp, R. et al. Radiotherapy plus concomitant and adjuvant temozolomide for glioblastoma. *N. Engl. J. Med.* **352**, 987–996 (2005).
2. Albert, N. L. et al. Response assessment in neuro-oncology working group and european association for neuro-oncology recommendations for the clinical use of PET imaging in gliomas. *Neuro Oncol.* **18**, 1199–1208 (2016).
3. Aldape, K. et al. Challenges to curing primary brain tumours. *Nat. Rev. Clin. Oncol.* **16**, 509–520 (2019).
4. Sanai, N. & Berger, M. S. Surgical oncology for gliomas: the state of the art. *Nat. Rev. Clin. Oncol.* **15**, 112–125 (2018).
5. Tang, T., Chang, B., Zhang, M. & Sun, T. Nanoprobe-mediated precise imaging and therapy of glioma. *Nanoscale Horiz.* **6**, 634–650 (2021).
6. Liu, Y. et al. Visualizing glioma margins by real-time tracking of gamma-glutamyltranspeptidase activity. *Biomaterials* **173**, 1–10 (2018).
7. Nguyen, Q. T. et al. Surgery with molecular fluorescence imaging using activatable cell-penetrating peptides decreases residual cancer and improves survival. *Proc. Natl. Acad. Sci. USA* **107**, 4317–4322 (2010).
8. Wu, Z. et al. Advances in magnetic resonance imaging contrast agents for glioblastoma-targeting theranostics. *Regenerative Biomater.* **8**, rbab062 (2021).
9. Li, D. et al. Visualization of diagnostic and therapeutic targets in glioma with molecular imaging. *Front Immunol.* **11**, 592389 (2020).
10. McCracken, D. J. et al. Turning on the light for brain tumor surgery: a 5-aminolevulinic acid story. *Neuro-Oncol.* **24**, S52–S61 (2022).
11. Shi, X. et al. PET/NIR-II fluorescence imaging and image-guided surgery of glioblastoma using a folate receptor alpha-targeted dual-modal nanoprobe. *Eur. J. Nucl. Med. Mol. Imaging* **49**, 4325–4337 (2022).
12. Shen, C. et al. Doxorubicin and indocyanine green loaded superparamagnetic iron oxide nanoparticles with PEGylated phospholipid coating for magnetic resonance with fluorescence imaging and chemotherapy of glioma. *Int. J. Nanomed.* **14**, 101–117 (2018).
13. Hu, Z. et al. First-in-human liver-tumour surgery guided by multispectral fluorescence imaging in the visible and near-infrared-I/II windows. *Nat. Biomed. Eng.* **4**, 259–271 (2019).
14. Cao, C. et al. Intraoperative near-infrared II window fluorescence imaging-assisted nephron-sparing surgery for complete resection of cystic renal masses. *Clin. Transl. Med.* **11**, e604 (2021).
15. Reddy, S., Tatiparti, K., Sau, S. & Iyer, A. K. Recent advances in nano delivery systems for blood-brain barrier (BBB) penetration and targeting of brain tumors. *Drug Discov. Today* **26**, 1944–1952 (2021).
16. Gao, H. et al. In situ formation of nanotheranostics to overcome the blood-brain barrier and enhance treatment of orthotopic glioma. *ACS Appl Mater. Interfaces* **12**, 26880–26892 (2020).
17. Han, S. et al. A novel synergetic targeting strategy for glioma therapy employing borneol combination with angiopep-2-modified, DOX-loaded PAMAM dendrimer. *J. Drug Target* **26**, 86–94 (2018).
18. Gallien, J. et al. Curcumin loaded dendrimers specifically reduce viability of glioblastoma cell lines. *Molecules* **26**, 6050 (2021).
19. Hernot, S., van Manen, L., Debie, P., Mieog, J. S. D. & Vahrmeijer, A. L. Latest developments in molecular tracers for fluorescence image-guided cancer surgery. *Lancet Oncol.* **20**, e354–e367 (2019).
20. Zhang, R. R. et al. Beyond the margins: real-time detection of cancer using targeted fluorophores. *Nat. Rev. Clin. Oncol.* **14**, 347–364 (2017).
21. Kasten, B. B. et al. Targeting MMP-14 for dual PET and fluorescence imaging of glioma in preclinical models. *Eur. J. Nucl. Med Mol. Imaging* **47**, 1412–1426 (2020).
22. Congdon, K. L. et al. Epidermal growth factor receptor and variant III targeted immunotherapy. *Neuro-Oncol.* **16**, viii20–viii25 (2014).
23. Hadjipanayis, C. G. et al. EGFRvIII antibody–conjugated iron oxide nanoparticles for magnetic resonance imaging–guided convection-enhanced delivery and targeted therapy of glioblastoma. *Cancer Res.* **70**, 6303–6312 (2010).
24. Elechalawar, C. K. et al. Dual targeting of folate receptor-expressing glioma tumor-associated macrophages and epithelial cells in the

brain using a carbon nanosphere–cationic folate nanoconjugate. *Nanoscale Adv.* **1**, 3555–3567 (2019).
25. Liu, K. et al. GCN5 potentiates glioma proliferation and invasion via STAT3 and AKT signaling pathways. *Int J. Mol. Sci.* **16**, 21897–21910 (2015).
26. Xiong, H. et al. Discovery of 1,8-acridinedione derivatives as novel GCN5 inhibitors via high throughput screening. *Eur. J. Med Chem.* **151**, 740–751 (2018).
27. Lee, J. Y. et al. Intraoperative near-infrared optical imaging can localize gadolinium-enhancing gliomas during surgery. *Neurosurgery* **79**, 856–871 (2016).
28. Li, B. et al. γ-Glutamyl transpeptidase-activable nanoprobe crosses the blood-brain barrier for immuno-sonodynamic therapy of glioma. *Nat. Commun.* **15**, 10418 (2024).
29. Leroueil, P. R. et al. Wide varieties of cationic nanoparticles induce defects in supported lipid bilayers. *Nano Lett.* **8**, 420–424 (2008).
30. Leroueil, P. R. et al. Nanoparticle interaction with biological membranes: does nanotechnology present a janus face? *Acc. Chem. Res.* **40**, 335–342 (2007).
31. Giesel, F. L., Mehndiratta, A. & Essig, M. High-relaxivity contrast-enhanced magnetic resonance neuroimaging: a review. *Eur. Radiol.* **20**, 2461–2474 (2010).
32. Liu, D. et al. LY6E protein facilitates adeno-associated virus crossing in a biomimetic chip model of the human blood-brain barrier. *Lab Chip* **22**, 4180–4190 (2022).
33. Zou, Y. et al. Brain co-delivery of temozolomide and cisplatin for combinatorial glioblastoma chemotherapy. *Adv. Mater.* **34**, e2203958 (2022).
34. Janjua, T. I. et al. Efficient delivery of Temozolomide using ultra-small large-pore silica nanoparticles for glioblastoma. *J. Controlled Release* **357**, 161–174 (2023).
35. Vorbrodt, A. W. Ultracytochemical characterization of anionic sites in the wall of brain capillaries. *J. Neurocytol.* **18**, 359–368 (1989).
36. Wu, D. et al. The blood–brain barrier: structure, regulation, and drug delivery. *Signal Transduct. Target. Ther.* **8**, 217 (2023).
37. Guo, Y. et al. Single-cell analysis reveals effective siRNA delivery in brain tumors with microbubble-enhanced ultrasound and cationic nanoparticles. *Sci. Adv.* **7**, eabf7390 (2021).
38. Chin, S. M. et al. Functional graphene for peritumoral brain microenvironment modulation therapy in glioblastoma. *Small* **19**, e2208227 (2023).
39. Soo Choi, H. et al. Renal clearance of quantum dots. *Nat. Biotechnol.* **25**, 1165–1170 (2007).
40. Yu, M. & Zheng, J. Clearance pathways and tumor targeting of imaging nanoparticles. *ACS Nano* **9**, 6655–6674 (2015).
41. Jenjob, R. et al. Enhanced conjugation stability and blood circulation time of macromolecular gadolinium-DTPA contrast agent. *Mater. Sci. Eng. C. Mater. Biol. Appl.* **61**, 659–664 (2016).
42. Min, H. S. et al. Systemic brain delivery of antisense oligonucleotides across the blood–brain barrier with a glucose-coated polymeric nanocarrier. *Angew. Chem. Int. Ed.* **59**, 8173–8180 (2020).
43. Chithrani, B. D. & Chan, W. C. Elucidating the mechanism of cellular uptake and removal of protein-coated gold nanoparticles of different sizes and shapes. *Nano Lett.* **7**, 1542–1550 (2007).
44. Zwain, T. et al. Overcoming biological barriers BBB/BBTB by designing PUFA functionalised lipid-based nanocarriers for glioblastoma targeted therapy. *Biomater. Adv.* **155**, 213660 (2023).
45. Hervé, F., Ghinea, N. & Scherrmann, J.-M. CNS delivery via adsorptive transcytosis. *AAPS J.* **10**, 455–472 (2008).
46. Zhang, H. et al. In vivo MR imaging of glioma recruitment of adoptive T-cells labeled with NaGdF(4) -TAT Nanoprobes. *Small* **14**, (2018).
47. Stylianopoulos, T., Soteriou, K., Fukumura, D. & Jain, R. K. Cationic nanoparticles have superior transvascular flux into solid tumors: insights from a mathematical model. *Ann. Biomed. Eng.* **41**, 68–77 (2013).
48. Wu, Y.-L. et al. Biophysical responses upon the interaction of nanomaterials with cellular interfaces. *Acc. Chem. Res.* **46**, 782–791 (2012).
49. Liu, D. et al. In vitro and in vivo studies on the transport of PEGylated silica nanoparticles across the blood-brain barrier. *ACS Appl Mater. Interfaces* **6**, 2131–2136 (2014).
50. Arvanitis, C. D., Ferraro, G. B. & Jain, R. K. The blood–brain barrier and blood–tumour barrier in brain tumours and metastases. *Nat. Rev. Cancer* **20**, 26–41 (2019).
51. Han, L. & Jiang, C. Evolution of blood–brain barrier in brain diseases and related systemic nanoscale brain-targeting drug delivery strategies. *Acta Pharmaceutica Sin. B* **11**, 2306–2325 (2021).
52. Slowing, I. I. et al. Exocytosis of mesoporous silica nanoparticles from mammalian cells: from asymmetric cell-to-cell transfer to protein harvesting. *Small* **7**, 1526–1532 (2011).
53. Liu, M. et al. Recent advances on small-molecule bromodomain-containing histone acetyltransferase inhibitors. *J. Medicinal Chem.* **66**, 1678–1699 (2023).
54. Shapira-Furman, T. et al. Biodegradable wafers releasing Temozolomide and Carmustine for the treatment of brain cancer. *J. Controlled Release* **295**, 93–101 (2019).

Acknowledgements

This work was financially supported by the Fundamental Research Funds for the Central Universities, Project No. YG2025ZD (T.J.), the National Natural Science Foundation of China, Project No. 91959125 (T.J.), 81972336 (T.J.), 81901804 (L.Z.), the International Cooperation Research Projects of Shanghai Science and Technology Commission, Project No. 19410740300 (T.J.), and the Fundamental research program funding of Ninth People's Hospital affiliated to Shanghai Jiao Tong university School of Medicine, Project No. JYZZ204(H.Z.), JYZZ191(Y.K.). We thank X.B. (First Affiliated Hospital of Army Medical University) for providing cell lines and D.L. (Huaqiao University) for providing guidance on the construction of the blood-brain barrier model.

Author contributions

T.J., H.Z., and L.Z. conceived and designed the project. H.Z., L.Z. synthesized and characterized the materials. X.B., Y.K., and Y.Y. performed all the cell and animal experiments. T.J., H.Z., L.Z., J.Z., X.B., and S.L. discussed the results, analyzed the data, and wrote the paper with the help of all authors. Q.L. and J.Z. supervised the research. All authors read and approved the final version of the manuscript.

Competing interests

The authors declare no competing interests.

Additional information

Supplementary information The online version contains supplementary material available at https://doi.org/10.1038/s41467-025-57598-9.

Correspondence and requests for materials should be addressed to Tianhai Ji.

Peer review information *Nature Communications* thanks Olaf van Tellingen, Jason Warram and the other, anonymous, reviewers for their contribution to the peer review of this work. A peer review file is available.